



Universiteit
Leiden
The Netherlands

CO2 reduction on post-transition metals and their alloys: an industrial approach

Pavesi, D.

Citation

Pavesi, D. (2022, April 20). *CO2 reduction on post-transition metals and their alloys: an industrial approach*. Retrieved from <https://hdl.handle.net/1887/3284964>

Version: Publisher's Version

License: [Licence agreement concerning inclusion of doctoral thesis in the Institutional Repository of the University of Leiden](#)

Downloaded from: <https://hdl.handle.net/1887/3284964>

Note: To cite this publication please use the final published version (if applicable).

6

Modulation of the selectivity of CO₂ to CO electroreduction in Palladium rich Palladium-Indium nanoparticles

This chapter is based on the article:

Pavesi, D., Dattila, F., Van de Poll, R. C. J., Anastasiadou, D., García-Muelas, R., Figueiredo, M., Gruter, G. J. M., López, N., Koper, M. T. M. & Schouten, K. J. P. Modulation of the selectivity of CO₂ to CO electroreduction in palladium rich Palladium-Indium nanoparticles. *J. Catal.*, 2021, 402, 229–237.

Abstract

Among the possible CO₂ reduction products, CO is of particular interest due to its large industrial applications. Transition metals in the Pt group are able to electrochemically reduce CO₂ to CO, but suffer from CO surface poisoning, which causes a quick deactivation and overall sluggish kinetics. Here, we show that by introducing In to Pd-rich bimetallic particles we can tune the selectivity and limit the surface poisoning of these catalysts. The addition of large amounts of In blocks CO₂ reduction activity and leads to a material selective for hydrogen evolution and insensitive to CO poisoning. This study provides insights into the dependence of CO₂ reduction selectivity on the composition of Pd-In nanoparticles, revealing the effect that different phases have on catalytic activity. The application of similar screenings to other bimetallic systems can potentially yield cheap, selective and poison-resistant catalysts for electrochemical applications.

6.1 Introduction

Typically, precious metals such as Au and Ag show high catalytic selectivity for the reduction of CO₂ to CO at room temperature.¹ Platinum group metals, instead, despite their ability to reduce CO₂ to CO, are prone to CO poisoning of the surface.² Carbon monoxide poisoning poses a problem also on Pt-based anode materials for fuel cell applications, where the incomplete oxidation of methanol or formic acid to CO₂ or the presence of CO in the H₂ stream can deactivate the electrocatalyst.^{3,4}

Pd has a peculiar behavior regarding CO evolution. Bulk Pd electrodes are reported to have low CO selectivity,^{1,5} while nanoparticles show high faradaic yields, although with sluggish kinetics.^{6,7} CO selectivity also depends on the size of Pd nanoparticles, with smaller particles being considerably more selective than bigger ones.⁸ Interestingly, in the case of bulk electrodes, the interaction between Pd and In has been reported to increase the selectivity towards CO evolution at the expense of current density.⁵

We show here that it is possible to modulate the CO poisoning of Pd-based electrocatalysts by introducing In. The formation of Pd-In solid solutions with low In content causes a small loss of selectivity compared to pure Pd, but accounts for an equal or slightly higher release-rate of surface adsorbed CO. Our experimental and theoretical evidences suggest that CO release may be facilitated on Pd sites adjacent to In sites on the Pd-In solid solution surface, while Pd domains remain susceptible to poisoning. The addition of excess In causes the formation of intermetallic Pd-In compounds with no selectivity towards CO₂ reduction products. This behavior is completely different from the one reported for bulk Pd-In electrodes. The use of a similar approach to favor the release of tightly bound CO or reduce poisoning for other metallic alloys nanoparticles can potentially

yield CO selective catalysts not based on precious metals, decreasing the capital costs of low temperature CO₂ to CO electrolyzers.

6.2 Experimental Section

6.2.1 Materials and chemicals. InCl₃ 99.999%, Trisodium Citrate dihydrate >99%, K₂PdCl₄ 99.99%, NaBH₄ 99.99% and Nafion™ solution (5 wt% solution in lower aliphatic alcohols and water (15-20% water content) were purchased from Aldrich. Vulcan carbon (VXC72R) was purchased from Cabot Corp. Carbon cloth (60% Teflon treated) was obtained from Fuel Cell Store. KHCO₃ 99.5% and H₂SO₄ 95% solution in water were purchased from Acros Organics.

6.2.2 Particle production and ink formulation. The particles supported on carbon were prepared in water *via* a chemical reduction method. The total amount of moles of metals was kept constant at 0.15 mmol and the ratios of In and Pd were varied in order to achieve different compositions. For the synthesis, an appropriate amount of solid InCl₃ was dissolved in about 1.5 mL of ultrapure water (Millipore 18.2 MΩ) along with 353 mg of Trisodium Citrate dihydrate, and a certain volume of a stock solution of 0.1M K₂PdCl₄. An overview of the different amounts of salts, as well as the different bimetallic compositions used in this study (indicated as atomic % in the catalyst denomination) can be found in Table 6.1. The resulting solution was diluted in 30 mL of ultrapure water to which 30 mg of carbon black were added under vigorous magnetic stirring. When the carbon was well dispersed in the liquid, the mixture was sonicated for 30 minutes and then placed back on the stirring plate. 7.5 mL of a 0.1M solution of NaBH₄ were added dropwise over the course of 5 minutes and the solution was left to react overnight. The calculated mass loading of metal on carbon was between 36.5% (In only) and 34.8% (Pd only). This number was obtained

assuming full reduction of the metal salts on the carbon support. For the ink formulation, an appropriate amount of carbon supported catalyst was suspended in ethanol by sonication. Afterwards, Nafion™ solution accounting for 20 wt% of the solids deposited on the electrode (dry catalyst + dry Nafion) was added under magnetic stirring. The ink was then sonicated again until homogenous and successively airbrushed on a 12 cm² carbon cloth support, from which we obtained the 1.5 cm² electrodes employed for the electrolysis and voltammetries. The values of electrode metal loading are reported in Table D1.

Catalyst Composition	Reagent Amounts	
	mg InCl ₃	μL 0.1M K ₂ PdCl ₄
In/C	33.17	0
Pd ₅₀ In ₅₀ /C	16.59	750
Pd ₉₀ In ₁₀ /C	3.31	1350
Pd ₉₈ In ₂ /C	0.8	1470
Pd/C	0	1500

Table 6.1. Ratios of salts used for synthesis. The catalysts are named after the atomic percent of the elements in the final material.

6.2.3 H-Cell electrolysis. The controlled potential electrolysis was carried out in an H-Cell connected to a Bio-logic MPG2 (with EC-lab software version 11.10) potentiostat. The catholyte was of 0.5 M KHCO₃ (100mL) and the anolyte was 0.5 M H₂SO₄ (100mL). The two chambers were separated by a reinforced Nafion© N324 membrane. The catholyte was continuously purged with CO₂ and stirred to ensure reactant availability on the electrode surface. The potential was applied on the working electrode (exposed area of 1.5 cm²) against a leak free Ag/AgCl

electrode and progressively stepped down from -0.5 to -1.25 V vs RHE (*iR*-corrected) in 30-minute steps. At the end of every step a sample of the catholyte was collected and analyzed for soluble products with an Agilent 1260 HPLC. Gas chromatography was performed on a Varian 4900 micro-GC equipped with four modules: CO_x module, MS5 (mol. sieve) module, PPQ (poraplotQ) module and 52C WAX module. The head space of the cell was automatically sampled every 4 minutes to detect gaseous products. All the potentials throughout this work will be referenced to the Reversible Hydrogen Electrode, unless otherwise specified.

6.2.4 Electrochemical measurements. Cyclic voltammetry was carried out in a cell connected to a Bio-logic MPG2 (with EC-lab software version 11.10) potentiostat. A leak free Ag/AgCl electrode was used as the reference electrode and the counter electrode was a Pt gauze. The working electrode was carbon cloth with the airbrushed catalytic ink. The electrolyte was a 0.5 M KHCO₃ solution, saturated with either CO₂ or N₂ before running the experiments. The electrodes, with an exposed area of 1.5 cm², were cycled at a scan rate of 50 mV/s with N₂ or CO₂ continuously purging the headspace of the cell. Cyclic voltammograms were also recorded directly after CO₂ reduction in the H-Cell for the Pd-rich catalysts in order to estimate the relative amounts of Pd sites on the surface of the particles from integration of the Pd(II) to Pd(0) reduction peak.

6.2.5 Particle characterization. X-Ray diffraction patterns of the particles supported on carbon were obtained by a Philips X'pert equipped with X'erator in a 2 θ range from 20 to 80 degrees. SEM was performed on an Apreo SEM equipped with an energy dispersive X-ray (EDX) analyzer. The analysis was performed to determine if the theoretical atomic ratios of Pd and In were obtained in the final product. The atomic ratios of Pd and In were measured in different parts of the carbon cloths and averaged to

obtain the final result. TEM imaging was performed on a FEI Tecnai 20 transmission electron microscope. X-ray photoelectron spectroscopy measurements were performed on the catalyst powders with a Thermo Fisher K-alpha instrument. The adsorption properties of the particles were investigated using CO as a probe molecule in the gas phase and recording difference Attenuated Total Reflectance (ATR) spectra. In order to do this, the catalyst inks prepared as described above were drop-cast on a Si hemisphere internal reflection element. The hemisphere was then mounted into a custom cell that allowed to control the composition of the headspace by flowing different gases and positioned into a Bruker Vertex 80 V Infrared spectrophotometer. The catalysts were pre-reduced in pure H₂ and after purging with Ar and recording a background spectrum the headspace of the cell was saturated with CO and difference spectra were collected. When a stable signal was obtained, the headspace of the cell was again purged with Ar in order to see the irreversibly adsorbed CO.

6.2.6 Computational details. Density functional theory (DFT) calculations were performed through the Vienna Ab Initio Simulation Package (VASP),^{9,10} using a plane-wave basis set and the Perdew–Burke–Ernzerhof (PBE) exchange-correlation functional.¹¹ Inner electrons were represented by the PAW formalism.^{12,13} The basis set cut-off energy was 450 eV. Throughout the whole study we model the experimentally synthesized nanoparticles following the Wulff theorem: the lower the surface energy of a given facet, the larger its surface extension on nanoparticles in the absence of an external potential.^{14,15} Thus, we first calculated the surface energy of several surface terminations and then assessed the adsorption of intermediates on the ones with lowest energies, expected to be the most abundant. Different supercells were considered to mimic the experimentally synthesized catalysts, namely: (i) metallic and intermetallic surfaces such as In(001), Pd(111),

PdIn(110), Pd₂In(010), Pd₃In(100); and (ii) In-Pd(111) solid solution. Structural relaxation was performed until the forces on the atoms were below 0.02 eV/Å. The Brillouin zone was sampled by a Γ -centered k-points mesh from the Monkhorst-Pack method,¹⁶ with a reciprocal grid size smaller than 0.03 Å⁻¹. For every model employed, the vacuum between the slabs was at least 10 Å. To assess CO₂ reduction, we placed reaction intermediates only on one side of the slabs, thus we included dipole correction in the simulations to remove spurious contributions from the asymmetric slab model.¹⁷ Adsorption energies were calculated including dispersion through the D2 method,^{18,19} with our reparametrization of the C₆ coefficients for metals.²⁰ Entropic terms at $T = 298.15$ K were considered to determine the Gibbs free energy profiles, whereas implicit solvation contributions were included through the VASP-MGCM framework.^{21,22}

6.3 Results

6.3.1 H-Cell Electrolysis. Fig. 6.1 summarizes the Faradaic Yield (FY) towards CO of the five investigated catalysts at four different potentials (bars) and the partial current density towards CO per Pd surface site (dots). To obtain this latter value, we measured a cyclic voltammogram immediately after electrolysis and we integrated the Pd(II) to Pd(0) reduction peak to calculate the reduction charge. Then, we estimated the moles of Pd on the electroactive surface from this reduction charge and finally we used this value to normalize the CO partial current. We applied this procedure to exclude any dependence of CO partial current density on particle size, catalyst loading or inhomogeneous distribution of the catalyst particles on the carbon cloth for Pd-rich systems. In fact, as can be seen in Fig. D1, the geometrical current density of the Pd₉₈In₂/C and Pd₉₀In₁₀/C is significantly higher than the pure Pd/C particles. The only other gaseous

product detected is H₂ for all the catalysts, as reported in Fig. D2 while In, as expected,¹ produces formate as the main CO₂ reduction product with a FY of about 70% at -0.95 V and 40% at -1.25 V. Pure Pd, as expected,⁷ also produces small amounts of formate at -0.5 V.

At mild cathodic bias, the CO selectivity correlates with particle composition, with Pd/C being the most selective and the other catalysts showing decreasing selectivity as a larger amount of In is present. In/C and Pd₅₀In₅₀/C do not produce CO in detectable amounts at any of the investigated potentials. Despite the voltammetric analysis showing the presence of CO poisoning on the surface of Pd/C, Pd₉₈In₂/C and Pd₉₀In₁₀/C (see Fig. 6.2), these catalysts evolve CO with appreciable selectivity. For example, at -0.75 V, the potential at which the highest CO selectivity is observed, pure Pd/C has a faradaic yield of about 80%, Pd₉₈In₂/C of about 70%, and Pd₉₀In₁₀/C of about 50%. For less negative potentials (-0.5 V), gaseous products were below the detection limit of the instrument due to the low currents achieved. On the other hand, the current density achieved at -1.25 V is very high for a H-cell (50-60 mA/cm²): this value is likely well above the CO₂ reduction limiting current in our conditions and it can potentially lead to degradation of the catalyst layer. This could explain the more erratic behavior of both the current density (Fig. D1) and the selectivity towards CO at this potential.

Despite the lower CO selectivity, for the Pd₉₈In₂/C system a higher partial current density towards CO is reached compared to Pd/C, both as geometrical current density (see Fig. D1) and as current density per Pd surface site. This especially holds at -0.95 V and -1.15 V, while this difference is less marked at -0.75 V and -1.25 V. Since, apart from the data point at -1.15 V, the partial current densities for Pd₉₈In₂/C and Pd/C are equivalent within the error bars, it is alternatively possible that, in spite of a decrease in selectivity, a similar CO partial current per Pd site is

6. Modulation of the selectivity of CO₂ to CO electroreduction in Palladium rich Palladium-Indium nanoparticles

retained. The CO partial current density then decreases on Pd₉₀In₁₀/C and goes to zero on Pd₅₀In₅₀/C.

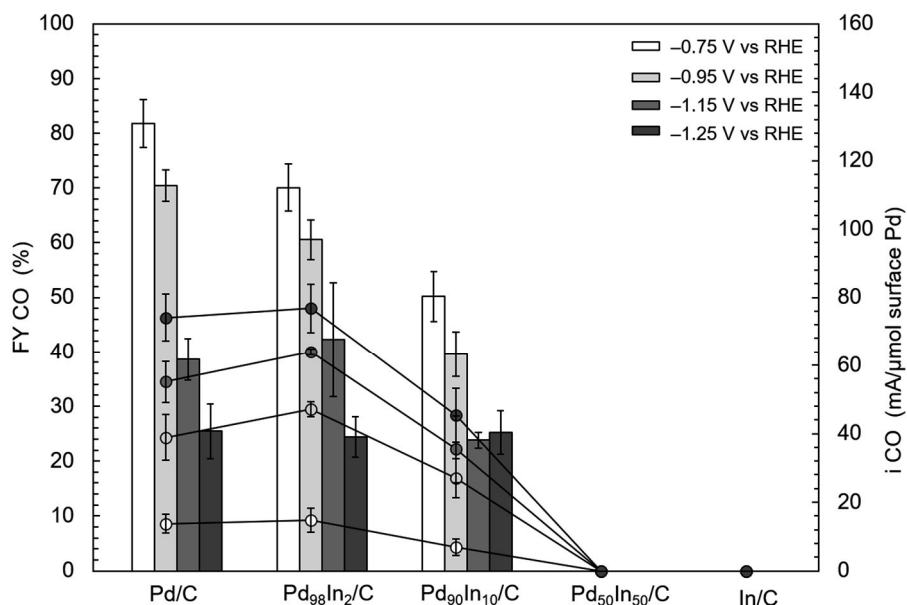


Figure 6.1. Faradaic yield towards CO for the five catalysts at four different potentials (bars) and partial current density towards CO per μmol of Pd on the electroactive surface (dots).

6.3.2 Electrochemical measurements. The electrodes were cycled at a scan rate of 50 mV/s in N₂ saturated and CO₂ saturated 0.5 M KHCO₃ between -1.5 and +1.3 V (before applying ohmic drop correction a posteriori), to allow the re-oxidation of CO adsorbed on the surface formed during the cathodic part of the voltammetry.

As shown in Fig. 6.2, the cathodic current density on Pd/C in CO₂ is significantly lower than for the N₂-saturated electrolyte, due to CO accumulation and consequent surface poisoning. In the

presence of CO₂, a reduction peak attributed to CO adsorption on the surface appears between approximately -0.1 and -0.7 V,⁶ whereas at potentials higher than $+0.5$ V the adsorbed CO is oxidized. On In/C nanoparticles the cathodic current density observed in CO₂ is significantly higher than in a N₂ saturated electrolyte because of the concomitant CO₂ reduction to formate.

As for the three bimetallic catalysts, they can be classified in two different groups according to their behavior: Pd₉₈In₂/C and Pd₉₀In₁₀/C behave roughly as Pd/C, while Pd₅₀In₅₀/C exhibits significant differences. For the Pd-rich bimetallics in CO₂ saturated electrolyte the large reducing peak assigned to CO adsorption is still present. However, its shape dramatically changes in the case of the Pd₉₈In₂/C system and the peak is broadened up until the most negative potential. In the case of Pd₉₀In₁₀/C the CO adsorption peak is more similar to Pd/C. Interestingly, while the cathodic current in CO₂ saturated electrolyte is significantly higher than Pd for both Pd₉₈In₂/C and Pd₉₀In₁₀/C, the current densities achieved in N₂ saturated electrolyte are very similar for these three catalysts. This may indicate the presence of active sites less susceptible to poisoning, which could contribute to a steeper rise in current on the bimetallic particles as more negative potentials are applied in the presence of CO₂. Instead, on Pd₅₀In₅₀/C the current densities in CO₂ and N₂ are not markedly different, and the CO adsorption peak is not prominent. Minor CO oxidation is only observable above $+0.5$ V, suggesting that some CO adsorbs on the surface, but still in lower amount than on pure Pd.

To confirm that CO adsorbs irreversibly on Pd/C, Pd₉₈In₂/C and Pd₉₀In₁₀/C, but not on Pd₅₀In₅₀/C and In/C, we performed cyclic voltammetries between -1.5 and $+0.6$ V, to avoid re-oxidation of surface adsorbed CO. The results are shown in Figs. D3a (first cycle) and D3b (last cycle). While during the first cycle the CO

6. Modulation of the selectivity of CO₂ to CO electroreduction in Palladium rich Palladium-Indium nanoparticles

adsorption peak is visible for Pd/C, Pd₉₈In₂/C and Pd₉₀In₁₀/C, from the second cycle the peak has disappeared and the voltammetric response is featureless, indicating that the surface of these three catalysts is subject to CO poisoning and fully covered after only one cycle if potentials where the oxidation of surface adsorbed CO are not reached. In the case of Pd₅₀In₅₀/C a minor adsorption peak is visible in the first cycle, but the shape of the voltammogram remains essentially the same, suggesting that the surface of this catalyst does not interact strongly with CO₂. In/C, as expected, does not adsorb CO.

In the case of Pd₉₈In₂/C and Pd₉₀In₁₀/C, the shape of the CV is similar to the one of Pd/C (especially in N₂ saturated electrolyte), with distortions and differences caused by the presence of In. In the case of Pd₅₀In₅₀/C the overall shape of the CV is markedly different from those of Pd/C or In/C, indicating that one or more intermetallic phases could be predominant.

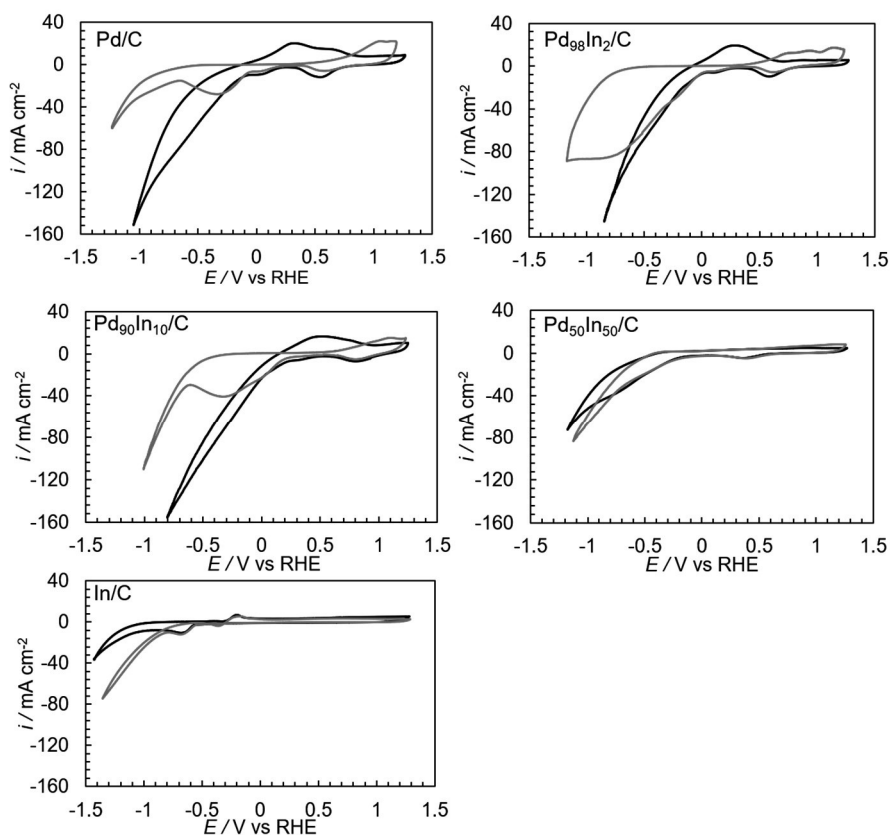


Figure 6.2. Cyclic voltammeteries (CVs) in N_2 saturated (black lines) and CO_2 saturated (gray lines) 0.5 M KHCO_3 .

6.3.3 Particle characterization. The atomic ratios of Pd and In in the catalysts were estimated with SEM-EDX and XPS, whereas the loading of metals on the carbon cloths was calculated by weighing the cloth before and after airbrushing. The atomic composition is very close to the value expected from the synthesis and electrode metal loading is almost constant for every system (Table D1).

6. Modulation of the selectivity of CO₂ to CO electroreduction in Palladium rich Palladium-Indium nanoparticles

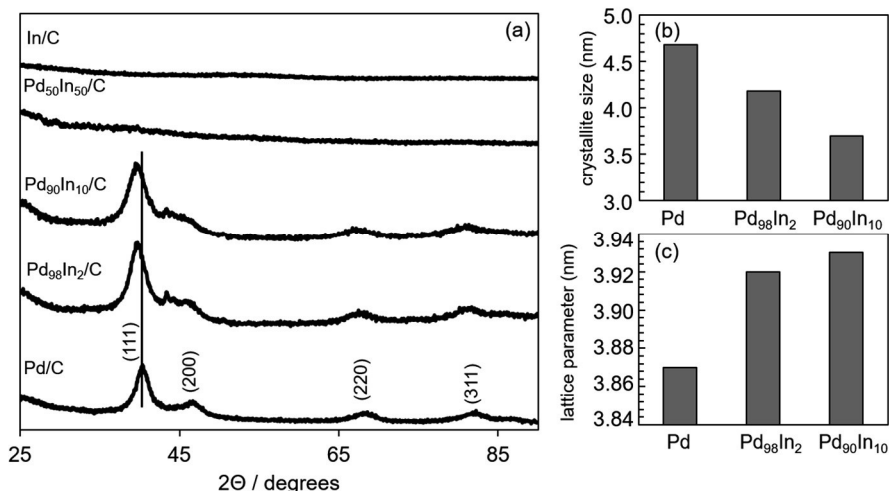


Figure 6.3. (a) X-Ray diffractograms of the investigated catalyst. (b) Crystallite size calculated using the Scherrer equation and (c) lattice parameter calculated using Bragg's law.

Fig. 6.3 shows the diffractograms of the materials in our study. In/C and Pd₅₀In₅₀/C give a flat signal, attributable to very small crystalline domains or to an amorphous nature. Pd/C, Pd₉₈In₂/C and Pd₉₀In₁₀/C show a nanocrystalline pattern with broad peaks. The crystallite sizes calculated with the Scherrer equation are 4.68 nm, 4.18 nm and 3.70 nm for Pd/C, Pd₉₈In₂/C and Pd₉₀In₁₀/C, respectively and are in good agreement with the sizes measured from the TEM images (Table D2) of 4.4 ± 1.2 nm for Pd, 4.1 ± 1.0 nm for Pd₉₈In₂ and 3.8 ± 1.0 nm for Pd₉₀In₁₀. Table D2 also reports the particle sizes of In/C (3.6 ± 0.9 nm) and Pd₅₀In₅₀/C (3.7 ± 0.4 nm), while representative TEM pictures are reported in Fig. D4. The diffractograms of Pd₉₈In₂/C and Pd₉₀In₁₀/C present peak shift compared to pure Pd, indicating the formation of a Pd-In solid solution, as is documented in this composition range.^{23,24} Correspondingly, the lattice parameter for the bimetallic particles increases. While a lattice expansion is reported upon formation of the solid solution phase, in bulk alloys

at 900°C the expansion is a linear function of In atomic % in Pd up to 17.6%.²⁴ In our case the expansion is similar for Pd₉₈In₂/C and Pd₉₀In₁₀/C. The amount of In soluble in Pd as random solid solution at room temperature is probably lower than 10%. This can cause the formation of a saturated solid solution phase and the demixing of excess In as small crystalline domains of ordered intermetallic Pd-In compounds, invisible to XRD due to the small size. The absence of an annealing treatment after the synthesis could be the cause of this more disordered structure. It is known that Pd and In can form several intermetallic compounds (for example Pd₃In, Pd₂In and PdIn) as well as solid solutions according to the composition range.²³ Increasing the amount of In increases the tendency to form these regular intermetallic structures over the disordered structure of substitutional alloys. This aspect is discussed in greater detail below.

Fig. 6.4 shows the ATR spectra of the five catalysts and a more detailed description of the ATR experiments can be found in Appendix D. In brief, Pd/C and Pd₉₈In₂/C do not show easily distinguishable behaviors in the binding energy or mode. This indicates that CO adsorbs very similarly on these nanoparticles when used as a probe molecule. This is in accordance with our DFT simulations (see discussion below and Fig. D9). Pd₉₀In₁₀/C shows deviations from the behavior of the other two Pd-rich catalysts in a CO atmosphere, with a higher prevalence of adsorption sites on top, but the spectrum is the same as the other two after stripping with Ar. This could imply that on these particles we have patches of new sites adsorbing CO weakly, but, after stripping with Ar, the CO left is adsorbed on strong binding sites analogous to the other two Pd-rich catalysts. This would suggest the existence of Pd-In solid solution domains and maybe intermetallic regions with a different adsorption behavior. This presence of solid solution plus small domains of intermetallic compounds for Pd₉₀In₁₀/C is partially expected since the In/Pd

6. Modulation of the selectivity of CO₂ to CO electroreduction in Palladium rich Palladium-Indium nanoparticles

ratio is only slightly above the solubility limit of In in Pd. Instead, Pd₅₀In₅₀/C adsorbs CO in a radically different way, only showing a weak band and In does not show any CO adsorption.

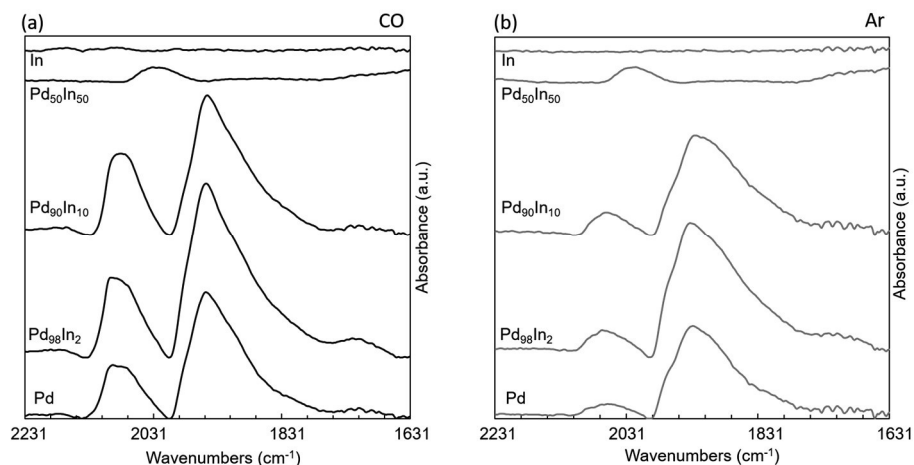


Figure 6.4. Difference ATR spectra for the adsorption of CO in the gas phase of the 5 different catalysts, after pre-reduction in pure H₂. (a) the spectra in CO atmosphere (irreversibly + reversibly adsorbed CO). (b) the spectra after purging the head space of the cell with Ar (irreversibly adsorbed CO). Peaks assigned according to Ref^[25].

It is remarkable that this CO adsorption/poisoning behavior is the same observed in the cyclic voltammetries, where Pd/C, Pd₉₈In₂/C and Pd₉₀In₁₀/C need an oxidative treatment to free the surface of CO (in the gas phase, since we do not control the potential, the adsorbed CO remains on the surface after Ar purging), while Pd₅₀In₅₀ only shows small amounts of CO oxidation and In does not show any CO poisoning at all. Some changes in the IR spectrum which might explain the different behavior shown during electrolysis start to be observable in Pd₉₀In₁₀/C and are evident in Pd₅₀In₅₀/C. Instead, in the case of Pd/C and Pd₉₈In₂/C no differences are easily noticeable when the surface is probed with CO, even though Pd₉₈In₂/C shows lower

selectivity and higher kinetics for CO evolution during electrolysis.

6.3.4 Adsorption of reaction intermediates. The particles investigated here, especially the ones selective towards CO evolution, are composed of pure Pd, a solid solution of In in Pd (as shown by XRD) and possibly small intermetallic domains. The bonds between In and Pd in the intermetallics are strong and partially covalent. Also, the tendency to form intermetallic compounds increases with increasing In content and it is likely that the Pd₅₀In₅₀ catalyst will be composed exclusively of intermetallic compounds at least after reduction.²³ The exact composition of these intermetallics is difficult to define since deviations from the thermodynamically most stable phase are common in bimetallic nanoparticle synthesis.^{26–29} The Computational Details in Appendix D show our analysis of the stability of the Pd_xIn_y systems against segregation and demixing of the solid solution. In summary, the formation of solid solutions and intermetallic compounds is energetically favorable (Table D3). Increasing the amount of In enhances the tendency of the solid solution phase to separate into a pure Pd phase + intermetallic compounds (Fig. D7). Indium substituents in a Pd matrix have a slight tendency to be on the surface and to be isolated, rather than forming In clusters (Fig. D8). Thus, we investigated two different kinds of systems by DFT simulations: (i) a solid solution of In in Pd modelled by substituting an In atom on the surface of a p(4×4) Pd(111) slab (Fig. 6.5) and (ii) three different intermetallic compounds expected in our composition range, PdIn, PdIn₂ and PdIn₃ (Fig. 6.6). The structures and lattice parameters of the model systems employed in this study are reported in Table D4. We note that the presence of In increases the interatomic metal-metal distance with respect to pure Pd, thereby accounting for the experimentally observed lattice expansion in Fig. 6.3c.

6. Modulation of the selectivity of CO₂ to CO electroreduction in Palladium rich Palladium-Indium nanoparticles

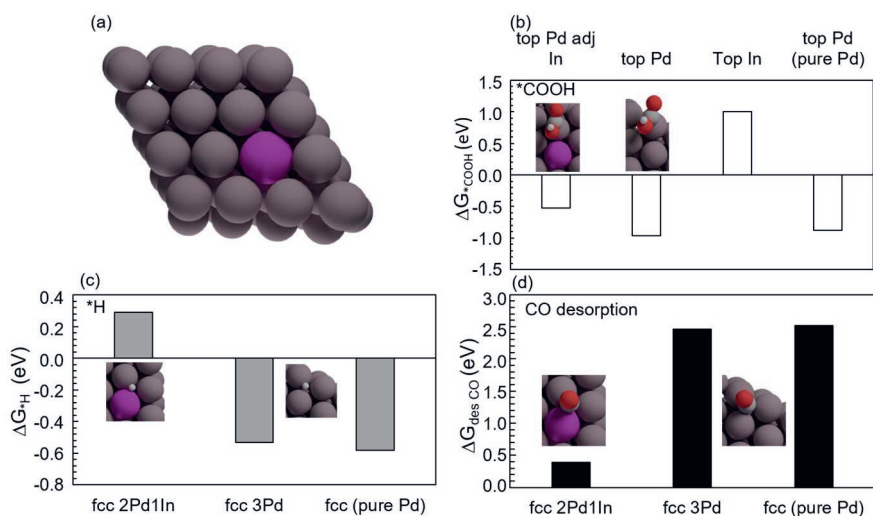


Figure 6.5. (a) Clean surface of the In-Pd p(4×4) (111) solid solution. (b) Binding energy of COOH and (c) H and (d) desorption energy of CO on different sites of the In-Pd p(4×4) (111) solid solution surface, compared to pure 4×4 Pd (111), at 1/16 ML surface coverage. Relevant COOH, H, and CO adsorption configurations on different surface sites of the solid solution are shown as insets. Pd atoms are represented in dark gray, In in purple, C in light gray, H in white and oxygen in red.

Figure 6.5 illustrates the binding energy of COOH and H as well as the desorption energy of CO for different adsorption sites on the Pd-In solid solution at 1/16 (0.06) ML surface coverage. Pd domains of the Pd-In solid solution behave as pure Pd sites for the adsorption of COOH and H and the desorption of CO. On the contrary, the adsorption of H on an fcc 2Pd1In hollow site is hindered ($\Delta G_{\text{H}} > 0$ eV), whilst the adsorption of COOH on a Pd in proximity of the In atom is exergonic ($\Delta G_{\text{COOH}}^* = -0.5$ eV). Furthermore, the In atom strongly favors CO desorption, since $\Delta G_{\text{des CO}}^*$ decreases from +2.46 (hollow site on pure Pd and Pd domains on the solid solution) to +0.39 eV (2Pd1In hollow site), enabling CO evolution.

Even though these low coverage results are already insightful, our models for Pd and Pd-In solid solution surfaces must be further extended to high CO coverages to mimic the Pd-rich surfaces during operation. Thus, we assessed 0.75 ML CO coverage *via* a (2×2)-3CO geometry (the most stable adsorption configuration on Pd(111) at this coverage³⁰) on both Pd(111) and Pd-In(111) solid solution. The results are shown in Fig. D9: the average CO desorption energy is almost equivalent for both cases and is about 1 eV lower than for the low coverage case due to CO-CO repulsion (+1.6 eV vs. +2.5 eV). The overall CO adsorption geometry does not change significantly upon presence of the In substituent, with the only difference that the two CO molecules close to In are repelled and thus move from a hollow to a bridge site (see Fig. D9). This theoretical evidence is consistent with the infrared spectra of Pd and Pd₉₈In₂. In fact, ATR spectra exhibit similar features for Pd and Pd₉₈In₂ (Fig. 6.4), since the local shift of CO molecules close to In from hollow to bridge adsorption sites could be hardly detectable due to the convolution of these peaks. Besides, the tendency of In atoms toward surface segregation (Fig. D8) is hindered at high CO coverage, since we calculate a thermodynamic driving force of – 1.1 eV for Pd to segregate at the surface and leave In atoms in the second layer. If In is present as a subsurface substituent, though, its weakening of intermediates binding is screened by the Pd matrix, leading to the absence of an outstanding difference in surface reactivity compared to a pure Pd slab (Fig. D10). Since the behavior of our Pd/C and Pd₉₈In₂/C regarding CO₂ reduction is noticeably different, we propose that Pd segregation does not fully remove In from the surface, at least at room temperature and on the short time-scale of our experiments. Nonetheless, this effect could play a relevant role in longer experiments or if these Pd-In materials were used for high-temperature experiments. During our ATR experiments, exposure to a high CO partial pressure could drive Pd surface

6. Modulation of the selectivity of CO₂ to CO electroreduction in Palladium rich Palladium-Indium nanoparticles

segregation to some extent, and this phenomenon could alternatively explain the very similar spectra for Pd/C and Pd₉₈In₂.

We can explain the weakening of H and CO binding energy on fcc 2PdIn hollow site through Bader charge analysis. The In atom embedded in the Pd matrix carries a partial positive charge of +0.64 |e⁻|, while electronic density is evenly distributed between the Pd neighbors. The positive polarization of the In substituent is due to the significantly different electronegativity between Pd and In (2.20 vs 1.78 on the Pauling scale, respectively). C atoms in the CO and COOH intermediates are respectively charged by +0.75 |e⁻| and +1.38 |e⁻|, thus we can expect an electrostatic repulsion between In site and adsorbate. In fact COOH adsorption on a pure In surface is slightly endergonic by +0.28 eV, while on a positively charged In atom embedded in the Pd surface it has a ΔG of about +1 eV. This positively charged In atom destabilizes CO and H adsorption, whereas the reactivity of Pd domains does not change since the increased electronic density is shared between many neighboring atoms. On top of this potential electrostatic repulsion, the In substituent weakens adsorption of intermediates due to the absence of d-orbitals in their valence shell. Overall, even though steps, corners, kinks and other geometric defects present on nanoparticles also alter the local electronic density, we expect these electrostatic and electronic effects to play a role for the reactivity of Pd-In solid solution.

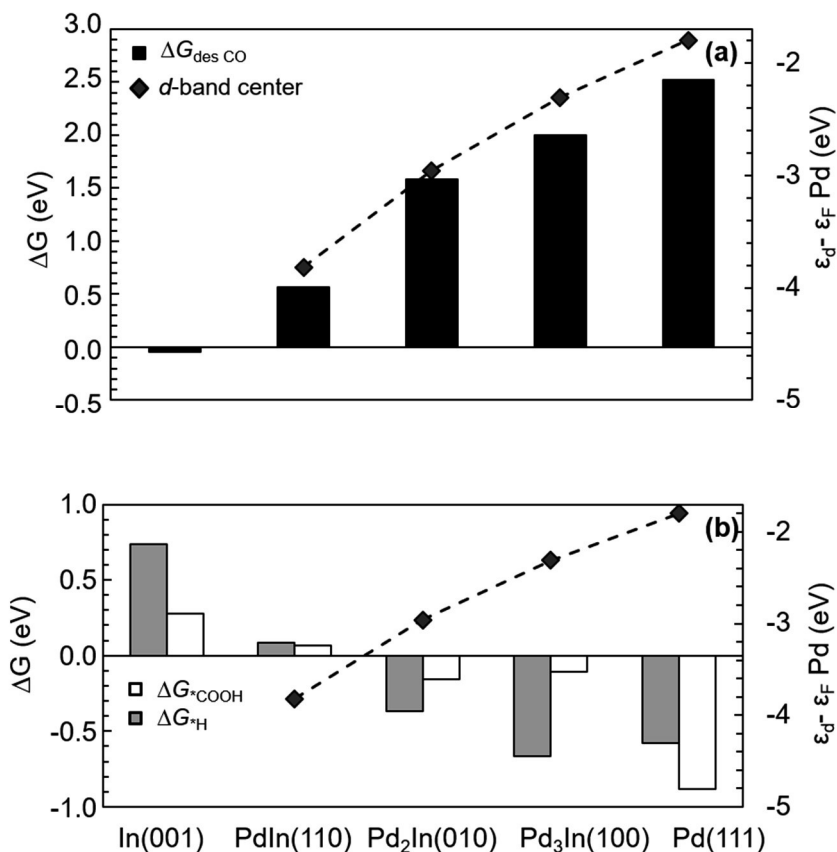


Figure 6.6. (a) Gibbs free energy for CO desorption (black bars) and (b) COOH and H adsorption (white and gray bars, respectively) on the most stable sites of the investigated intermetallic compounds. The d -band center of Pd for the different metals and intermetallic compounds is also shown.

The intermetallic systems show a completely different catalytic behavior. Fig. 6.6 shows a comparison of Gibbs free energy for CO desorption (panel a, black bars), COOH and H adsorption (panel b, white and gray bars, respectively) on the most stable terminations of the investigated intermetallic compounds as well

as pure Pd and In. Different terminations as well as different adsorption configurations have been considered and are reported in Tables D5-D6. In Fig. 6.5, the *d*-band center of pure Pd and those of Pd in the intermetallic compounds are also plotted for completeness. While for the solid solution the *d*-band center does not change significantly (−1.81 eV on pure Pd vs −1.79 eV on Pd sites adjacent to the In substituent, not reported in Fig. 6.6), for the intermetallic compounds this parameter shifts to more negative values due to structural changes, Pd isolation and formation of partially covalent bonds with increasing amount of In. The *d*-band center shifts to lower energies and this causes a progressive weakening of CO adsorption energy as expected from the *d*-band model,^{31–33} although never to the levels of the solid solution system in proximity of the In atom. The binding energies of H and COOH also change with increasing In content: while pure Pd binds COOH more strongly than H, the situation is reversed for Pd₃In and Pd₂In. The compound PdIn shows similar positive binding energies for both intermediates.

6.4 Discussion

The dependence of the CO selectivity of In-Pd systems on In content must be rationalized by addressing (i) why pure Pd nanoparticles are evolving CO with such high selectivity and (ii) the reactivity of solid solutions, intermetallic compounds or their interplay, given the Pd-In phase diagram and the experimental and theoretical characterization reported previously.

6.4.1 Pd. Pure Pd binds CO very strongly, in fact the computed binding energy, even at high coverage, is very high and makes the desorption of this molecule from the surface very endergonic. On bulk Pd electrodes, the reported selectivity towards CO is generally low (around 25%)^{1,5} and CO poisoning occurs, leading to a high-overpotential hydrogen evolution as the main electrochemical reaction. The situation is different on carbon

supported nanoparticles, especially smaller ones in the range of 2.5 to 4.5 nm,⁸ where high CO selectivity can be achieved during steady state electrolysis, despite the high CO coverage and the sluggish kinetics.^{6,7} Hydrogen evolution is instead hindered by CO surface poisoning, thus motivating the high selectivity toward CO. Thus, a small number of sites with lower CO affinity exist on the surface of Pd catalysts that can either produce and release CO or alternatively facilitate the desorption of CO formed on crystalline Pd sites. The nature of these active sites is not clear, but some inspiration can be drawn from the field of heterogenous catalysis, where the *in-operando* formation of Pd carbides, either from the carbon support or from the carbonaceous reactants can cause the formation of sites with considerably lower binding energy for catalytic intermediates, favoring, for example, partial hydrogenation rather than full hydrogenation of hydrocarbons.^{34–37}

6.4.2 Pd-In solid solutions. The experimental and theoretical analyses presented above suggest that the presence of In as a solid solution surface substituent, such as in Pd₉₈In₂, is neither drastically altering CO binding nor its adsorption configuration at high CO coverages (Fig. 6.4 and Fig. D9). Nonetheless, the presence of this positively charged In substituent changes the adsorption properties in its surroundings by creating sites with weaker binding energies for *H and *COOH (on top of In) and lower desorption energy for CO (Fig. 6.5). While when using CO as a probe molecule these sites may be avoided by slightly rearranging the adsorption geometry (Fig. D9), during electrolysis these weak CO binding sites close to the In impurity would present a locally lower CO coverage and remain more accessible for electrochemical reactions since the Pd-rich domains will be covered by tightly bound CO. The catalytic behavior of these weak-CO-binding Pd-In sites is not clear-cut and could be influenced by many other factors. They could be

selective to hydrogen evolution due to the steric repulsion at high CO coverages, or they may also enable CO formation due to their less endergonic CO desorption energy and favorable COOH adsorption on top a Pd atom adjacent to the In atom. This can explain the experimental behavior displayed by Pd/C and Pd₉₈In₂/C regarding the CO partial current. We expect CO₂ reduction to CO to occur more easily around an In substituent due to the almost thermoneutral CO desorption, which could cause higher overall currents. On the other hand, the lower CO poisoning and steric limitations could promote HER, causing loss of selectivity. In any case, due to the low content of In on the surface and potential Pd surface segregation, the possible promoting effect on CO₂R activity may be limited, thus motivating partial current densities per electroactive Pd for Pd/C and Pd₉₈In₂/C being equivalent within the error bars.

6.4.3 Intermetallic compounds. As presented in Fig. 6.6, the formation of intermetallic compounds favors hydrogen evolution. By comparing *H and *COOH binding energy on Pd and the intermetallic compounds within our compositional range, we can see that Pd binds COOH more strongly than H, thus leading to high CO coverage. Instead, Pd₃In and Pd₂In will likely catalyze hydrogen evolution, since these intermetallics exhibit stronger affinity for H rather than COOH, resulting in a higher *H coverage. The PdIn compound, instead, presents slightly endergonic binding energies for both *H and *COOH. In this case HER should be favored due to the larger water content in the electrolyte, however the hydrogen evolution catalyst will be suboptimal. In fact, despite the absence of CO poisoning, only a sluggish hydrogen evolution is observed on Pd₅₀In₅₀, for which we expect to have the highest amount of intermetallic compounds and possibly the compound PdIn. On Pd₉₀In₁₀, where we expect to have both solid solution and intermetallic phases, we have a somewhat intermediate behavior.

Previous results³⁸ have shown that the presence of Pd in In-rich bimetallic particles can decrease the selectivity of the In system for the reduction of CO₂ to formate. Combined with the present results, we provide a comprehensive investigation of the evolution of the behavior of Pd-In bimetallic nanoparticles in regard to the electroreduction of CO₂. Pure In is selective to formate, while the addition of even small amounts of Pd lowers CO₂ reduction selectivity, favoring hydrogen evolution. This happens because the solubility of Pd in the In matrix is very low, and even small amounts of Pd result in the formation of intermetallic compounds in an In matrix. Increasing amounts of Pd should result in the exclusive formation of intermetallic compounds, selective to hydrogen evolution. This is what we observe in the central region of the composition range. On the other hand, In is partially soluble in the Pd matrix, and this yields CO-selective electrocatalysts (although less selective than pure Pd) based on Pd-In solid solutions with slightly enhanced kinetics.

While we have strong evidence that the formation of Pd-In intermetallic compounds is detrimental to CO₂ electroreduction in general, it is hard to understand which intermetallic compounds are specifically formed in the nanoparticles. As mentioned above, the formation of these intermetallic structures, especially when using low temperature synthetic methods, can be kinetically controlled, leading to deviations from the most thermodynamically stable phase according to the phase diagram. For instance, the preferential formation of the PdIn compounds with a CsCl structure has been reported even in In-rich compositional ranges.^{29,39} Interestingly, Pd-In intermetallic compounds have been previously reported to be selective for ethane dehydrogenation and CO₂ hydrogenation to methanol using thermal catalysis.^{29,39,40} Moreover, the selective electroreduction of CO₂ to CO on Pd-In bimetallic bulk electrodes

has been demonstrated.⁵ Therefore, the behavior of these compounds is different not only when used as heterogenous catalysts or electrocatalysts but also going from bulk to nanoparticulate electrodes.

6.5 Conclusions

We have shown that the interaction of In and Pd in Pd-In bimetallic catalysts can yield several different phases and that the selectivity of the electroreduction of CO₂ can change dramatically depending on the catalytic phase, ranging from formate on In, to HER on Pd-In intermetallics and finally to CO evolution on Pd and Pd-In solid solutions. Interestingly, Pd-In intermetallic compounds do not interact with CO₂ in electrochemical conditions, whereas they are able to hydrogenate CO₂ to methanol under thermocatalytic conditions. Such complex and tunable behavior in the case of the Pd-In nanoparticles warrants the investigation of similar bimetallic systems to find cheaper, more selective and stable catalysts for future applications. Also, understanding the effect of the electrochemical environment on the catalytic process can help shedding light on the very different behavior of intermetallic compounds in thermal and electro-catalysis.

References

- (1) Hori, Y. Electrochemical CO₂ Reduction on Metal Electrodes, *Modern Aspects of Electrochemistry*. 2008, 89–189.
- (2) Darby, M. T., Sykes, E. C. H., Michaelides, A. & Stamatakis, M. Carbon Monoxide Poisoning Resistance and Structural Stability of Single Atom Alloys. *Top. Catal.*, 2018, 61, 428–438.
- (3) Cheng, X., Shi, Z., Glass, N., Zhang, L., Zhang, J., Song, D., Liu, Z. S., Wang, H. & Shen, J. A review of PEM hydrogen fuel cell contamination: Impacts, mechanisms, and mitigation. *J. Power Sources*, 2007, 165, 739–756.
- (4) Chung, D. Y., Kim, H. II, Chung, Y. H., Lee, M. J., Yoo, S. J., Bokare, A. D., Choi, W. & Sung, Y. E. Inhibition of CO poisoning on Pt catalyst coupled with the reduction of toxic hexavalent chromium in a dual-functional fuel cell. *Sci. Rep.*, 2014, 4, 1–5.
- (5) Luo, W., Xie, W., Li, M., Zhang, J. & Züttel, A. 3D hierarchical porous indium catalyst for highly efficient electroreduction of CO₂. *J. Mater. Chem. A*, 2019, 7, 4505–4515.
- (6) Guo, R. H., Liu, C. F., Wei, T. C. & Hu, C. C. Electrochemical behavior of CO₂ reduction on palladium nanoparticles: Dependence of adsorbed CO on electrode potential. *Electrochem. commun.*, 2017, 80, 24–28.
- (7) Min, X. & Kanan, M. W. Pd-Catalyzed Electrohydrogenation of Carbon Dioxide to Formate: High Mass Activity at Low Overpotential and Identification of the Deactivation Pathway. *J. Am. Chem. Soc.*, 2015, 137, 4701–4708.
- (8) Gao, D., Zhou, H., Wang, J., Miao, S., Yang, F., Wang, G., Wang, J. & Bao, X. Size-Dependent Electrocatalytic Reduction of CO₂ over Pd Nanoparticles. *J. Am. Chem. Soc.*, 2015, 137, 4288–4291.
- (9) Kresse, G. & Furthmüller, J. Efficient iterative schemes for ab initio total-energy calculations using a plane-wave basis set. *Phys. Rev. B*, 1996, 54, 11169–11186.
- (10) Kresse, G. & Furthmüller, J. Efficiency of ab-initio total energy calculations for metals and semiconductors using

6. Modulation of the selectivity of CO₂ to CO electroreduction in Palladium rich Palladium-Indium nanoparticles

- a plane-wave basis set. *Comput. Mater. Sci.*, 1996, 6, 15–50.
- (11) Perdew, J. P., Burke, K. & Ernzerhof, M. Generalized Gradient Approximation Made Simple. *Phys. Rev. Lett.*, 1996, 77, 3865–3868.
- (12) Blöchl, P. E. Projector augmented-wave method. *Phys. Rev. B*, 1994, 50, 17953–17979.
- (13) Kresse, G. & Joubert, D. From ultrasoft pseudopotentials to the projector augmented-wave method. *Phys. Rev. B*, 1999, 59, 1758–1775.
- (14) Wulff, G. XXV. Zur Frage der Geschwindigkeit des Wachstums und der Auflösung der Krystallflächen. *Zeitschrift für Krist. - Cryst. Mater.*, 1901, 34, 449–530.
- (15) Carchini, G., Almora-Barrios, N., Revilla-López, G., Bellarosa, L., García-Muelas, R., García-Melchor, M., Pogodin, S., Błoński, P. & López, N. How theoretical simulations can address the structure and activity of nanoparticles. *Top. Catal.*, 2013, 56, 1262–1272.
- (16) Monkhorst, H. J. & Pack, J. D. Special points for Brillouin-zone integrations. *Phys. Rev. B*, 1976, 13, 5188–5192.
- (17) Makov, G. & Payne, M. C. Periodic boundary conditions in ab initio calculations. *Phys. Rev. B*, 1995, 51, 4014–4022.
- (18) Grimme, S. Semiempirical GGA-type density functional constructed with a long-range dispersion correction. *J. Comput. Chem.*, 2006, 27, 1787–1799.
- (19) Bučko, T., Hafner, J., Lebègue, S. & Ángyán, J. G. Improved Description of the Structure of Molecular and Layered Crystals: Ab Initio DFT Calculations with van der Waals Corrections. *J. Phys. Chem. A*, 2010, 114, 11814–11824.
- (20) Almora-Barrios, N., Carchini, G., Błoński, P. & López, N. Costless Derivation of Dispersion Coefficients for Metal Surfaces. *J. Chem. Theory Comput.*, 2014, 10, 5002–5009.
- (21) Garcia-Ratés, M. & López, N. Multigrid-Based Methodology for Implicit Solvation Models in Periodic DFT. *J. Chem. Theory Comput.*, 2016, 12, 1331–1341.
- (22) Garcia-Ratés, M., García-Muelas, R. & López, N. Solvation Effects on Methanol Decomposition on Pd(111),

- Pt(111), and Ru(0001). *J. Phys. Chem. C*, 2017, 121, 13803–13809.
- (23) Knight, J. R. & Rhys, D. W. The systems palladium - indium and palladium - tin. *J. Less-Common Met.*, 1959, 1, 292–303.
- (24) Harris, I. R., Norman, M. & Bryant, A. W. A study of some palladium-indium, platinum-indium and platinum-tin alloys. *J. Less-Common Met.*, 1968, 16, 427–440.
- (25) Ebbesen, S. D., Mojet, B. L. & Lefferts, L. The influence of water and pH on adsorption and oxidation of CO on Pd/Al₂O₃-an investigation by attenuated total reflection infrared spectroscopy. *Phys. Chem. Chem. Phys.*, 2009, 11, 641–649.
- (26) Gallagher, J. R., Childers, D. J., Zhao, H., Winans, R. E., Meyer, R. J. & Miller, J. T. Structural evolution of an intermetallic Pd–Zn catalyst selective for propane dehydrogenation. *Phys. Chem. Chem. Phys.*, 2015, 17, 28144–28153.
- (27) Iwasa, N. & Takezawa, N. New supported Pd and Pt alloy catalysts for steam reforming and dehydrogenation of methanol. *Top. Catal.*, 2003, 22, 215–224.
- (28) Takanashi, T., Tamura, M., Nakagawa, Y. & Tomishige, K. Structure of catalytically active Rh–In bimetallic phase for amination of alcohols. *RSC Adv.*, 2014, 4, 28664–28672.
- (29) Wu, Z., Wegener, E. C., Tseng, H. T., Gallagher, J. R., Harris, J. W., Diaz, R. E., Ren, Y., Ribeiro, F. H. & Miller, J. T. Pd-In intermetallic alloy nanoparticles: Highly selective ethane dehydrogenation catalysts. *Catal. Sci. Technol.*, 2016, 6, 6965–6976.
- (30) Rose, M. K., Mitsui, T., Dunphy, J., Borg, A., Ogletree, D. F., Salmeron, M. & Sautet, P. Ordered structures of CO on Pd(111) studied by STM. *Surf. Sci.*, 2002, 512, 48–60.
- (31) Robinson, P. J. & Holbrook, K. A. Why gold is the noblest of all the metals. *Nature*, 1995, 376, 238–240.
- (32) Hammer, B. & Nørskov, J. K. Electronic factors determining the reactivity of metal surfaces. *Surf. Sci.*, 1995, 343, 211–220.
- (33) Lopez, N., TVW, J., BS, C., Xu, Y., Mavrikakis, M., Bligaard, T. & JK, N. On the origin of the catalytic activity

6. Modulation of the selectivity of CO₂ to CO electroreduction in Palladium rich Palladium-Indium nanoparticles

- of gold nanoparticles for low-temperature CO oxidation. *J. Catal.*, 2004, 223, 232–235.
- (34) Collett, C. H. & McGregor, J. Things go better with coke: The beneficial role of carbonaceous deposits in heterogeneous catalysis. *Catal. Sci. Technol.*, 2016, 6, 363–378.
- (35) Tew, M. W., Nachtegaal, M., Janousch, M., Huthwelker, T. & Van Bokhoven, J. A. The irreversible formation of palladium carbide during hydrogenation of 1-pentyne over silica-supported palladium nanoparticles: In situ Pd K and L 3 edge XAS. *Phys. Chem. Chem. Phys.*, 2012, 14, 5761–5768.
- (36) Studt, F., Abild-Pedersen, F., Bligaard, T., Sørensen, R. Z., Christensen, C. H. & Nørskov, J. K. On the role of surface modifications of palladium catalysts in the selective hydrogenation of acetylene. *Angew. Chemie - Int. Ed.*, 2008, 47, 9299–9302.
- (37) Bugaev, A. L., Guda, A. A., Pankin, I. A., Groppo, E., Pellegrini, R., Longo, A., Soldatov, A. V. & Lamberti, C. The role of palladium carbides in the catalytic hydrogenation of ethylene over supported palladium nanoparticles. *Catal. Today*, 2019, 336, 40–44.
- (38) Pavesi, D., Ali, F. S. M., Anastasiadou, D., Kallio, T., Figueiredo, M., Gruter, G.-J. M., Koper, M. T. M. & Schouten, K. J. P. CO₂ electroreduction on bimetallic Pd–In nanoparticles. *Catal. Sci. Technol.*, 2020, 10, 4264–4270.
- (39) García-Trenco, A., Regoutz, A., White, E. R., Payne, D. J., Shaffer, M. S. P. & Williams, C. K. PdIn intermetallic nanoparticles for the Hydrogenation of CO₂ to Methanol. *Appl. Catal. B Environ.*, 2018, 220, 9–18.
- (40) Frei, M. S., Mondelli, C., García-Muelas, R., Kley, K. S., Puértolas, B., López, N., Safonova, O. V., Stewart, J. A., Curulla Ferré, D. & Pérez-Ramírez, J. Atomic-scale engineering of indium oxide promotion by palladium for methanol production via CO₂ hydrogenation. *Nat. Commun.*, 2019, 10, 1–11.